Characteristics of magma-driven hydrothermal systems at oceanic spreading centers

Robert P. Lowell and Aida Farough
Department of Geosciences, Virginia Tech, Blacksburg, Virginia, USA (rlowell@vt.edu)

Joshua Hoover
Department of Geosciences, Virginia Tech, Blacksburg, Virginia, USA

Now at Department of Meteorology, Pennsylvania State University, College Park, Pennsylvania, USA

Kylin Cummings
Department of Geosciences, Virginia Tech, Blacksburg, Virginia, USA

Department of Anthropology, New Mexico State University, Las Cruces, New Mexico, USA

[1] We use one- and two-limb single-pass models to de termine vent field characteristics such as mass flow rate Q, bulk permeability in the discharge zone k_d, thickness of the conductive boundary layer at the base of the system δ, magma replenishment rate, and residence time in the discharge zone. Data on vent temperature, vent field area, heat output, and the surface area and depth of the subaxial magma chamber (AMC) constrain the models. The results give $Q \sim 100 \, \text{kg/s}$, $k_d \sim 10^{-13} \, \text{m}^2$, and $\delta \sim 10 \, \text{m}$, essentially independent of spreading rate, and detailed characteristics of the AMC. In addition, we find no correlation between heat output at individual vent fields and spreading rate or depth to the AMC. We conclude that high-temperature hydrothermal systems are driven by local magma supply rates in excess of that needed for steady state crustal production and that crustal permeability enables hydrothermal circulation to tap magmatic heat regardless of AMC depth. Using data on partitioning of heat flow between focused and diffuse flow, we find that 80–90% of the hydrothermal heat output is derived from high-temperature fluid, even though much of the heat output discharges as low-temperature fluid. In some cases, diffuse flow fluids may exhibit considerable conductive cooling or heating. By assuming conservative mixing of diffuse flow fluids at East Pacific Rise 9°50′N, we find that most transport of metals such as Fe and Mn occurs in diffuse flow and that CO_2, H_2, and CH_4 are taken up by microbial activity.

1. Introduction

[2] Seafloor hydrothermal systems are an important component of Earth's dynamic heat engine [e.g., *Sclater et al.*, 1980; *Stein and Stein*, 1994] and an important driver of its geochemical cycles [e.g., *Wolery and Sleep*, 1976; *Elderfield and Schultz*, 1996]. At oceanic spreading centers seawater percolates downward into the crust where it is primarily heated by magma and rises to the seafloor where it escapes in the form of high-temperature black smoker vents and associated diffuse discharge. Fluid circulation in these high-temperature systems involves complex water-rock chemical reactions and phase separation. Consequently, numerical modeling of reactive transport in multicomponent, multiphase systems is required to obtain a full understanding of the characteristics and evolution of seafloor hydrothermal systems [e.g., *Lowell et al.*, 2008]. *Lowell and Germanovich* [1994, 2004] have shown, however, that relatively simple scaling laws can provide significant insight into the physics of seafloor hydrothermal systems. Their approach used generic values for hydrothermal heat output, vent temperature, area of a hydrothermal field, and planform area of a subaxial magma chamber (AMC) to characterize a number of key hydrothermal parameters. *Lowell* [2010] and *Lowell et al.* [2012] applied the method to a number of hydrothermal systems at slow-spreading ridges and at 9°50′N on the East Pacific Rise (EPR), respectively.

[3] In this paper, we apply the classical single-pass modeling approach to all seafloor hydrothermal systems for which the constraining data are available and compile the estimates of mass flow, bulk permeability of the discharge zone, boundary layer thickness, magma replenishment rate, and fluid residence time in the discharge zone. By using the observational data directly to constrain subsurface parameters that are difficult to measure, we are actually performing an inverse problem. This approach is in direct contrast to numerical cellular convection models that assume values of permeability, prescribe boundary conditions, and solve for flow patterns and temperature distributions. Table 1 lists the hydrothermal sites used and provides the basic input data needed to construct the models along with the spreading rate and depth to the AMC (Additional details about these hydrothermal sites can be obtained from http://www.interridge.org/irvents/ventfields_list_all). In addition, we use a two-limb

single-pass model to determine the mean fraction of high-temperature fluid incorporated into diffuse flow and to calculate chemical transports in focused and diffuse flow at the vent field scale. The data on heat output, mean vent temperature, and Mg concentration for both high-temperature and diffuse flow fluid required for this exercise are only available for Axial Seamount Hydrothermal Emissions Study (ASHES) and Main Endeavour (MEF) fields on the Juan de Fuca Ridge (JDFR), Lucky Strike on the Mid-Atlantic Ridge (MAR), and 9°50′N on the EPR (Table 1). Finally, we plot hydrothermal heat output as a function of spreading rate and depth to the AMC for sites with available data. We find that there is essentially no correlation among these parameters, suggesting that localized magma supply and crustal permeability exert primary control of hydrothermal heat output at a given site.

[4] After more than two decades of intense focused study on seafloor hydrothermal systems, our knowledge of these systems is still very limited. Much of the key data needed to constrain quantitative models are either missing or subject to considerable uncertainty, as discussed in section 4.1. Despite these drawbacks, we believe that the estimates provided in this paper enhance fundamental understanding of the physics of magma-driven hydrothermal circulation in the oceanic crust. The modeling approach used here points to the need for additional data on the spatial and temporal evolution of the AMC and hydrothermal heat output as well as better constraints on the subsurface plumbing system.

2. Single-Pass Modeling of Seafloor Hydrothermal Systems

2.1. The Classical Single-Pass Model

[5] In the classical single-pass model of a hydrothermal circulation system conservation of mass, momentum and energy are expressed in terms of total mass flow Q, mean fluid discharge temperature T_d, and advective heat output H at the vent field scale as fluid circulation occurs through discrete circulation pathways [e.g., *Elder*, 1981]. For a magma-driven seafloor hydrothermal system these pathways generally consist of a deep recharge zone, a cross-flow zone that transfers heat by conduction across a thermal boundary layer from a subjacent convecting, crystallizing AMC,

Table 1. Principal Observables Used to Constrain Single-Pass Hydrothermal Model Parameters Q, k, δ, $\dot{V}_m$, and τ that are Calculated in Table 2[a]

		Site	A_d[b] (m²)	$T_{d(ht)}$[c] (°C)	H[d] (MW)	H_4/H_3	T_4 (°C)	A_m[e] (m²)	Depth to Magma Chamber h (km)	Full Spreading Rate (mm/a)
Integrated measurements	MAR	Rainbow[f]	3.0E+04	364	500	0				21
		Broken Spur[g]	5.0E+03	365	28					24
		TAG[h]	3.0E+04	364	1700				>7	24
	JDFR	Southern cleft[i]	1.0E+05	350	193			2.0E+06	2	56
		Northern cleft[j]	1.0E+05	324	551			2.0E+06	2.3	56
		Salty Dawg[k]	1.0E+03	310	50			1.0E+06	2.2–2.4	55
		High Rise[l]	1.6E+05	330	500			1.0E+06	2.1–2.3	55
		MEF[m]	6.0E+04	365	450	1	29	1.0E+06	2.1–2.5	55
		Mothra[n]	5.0E+04	275	100			1.0E+06	2.5–3.1	55
Point measurements	EPR	9°50′N[o]	1.0E+04	371	160	7	29	1.0E+06	1.5	110
		21°N[p]	5.5E+03	350	200					60
	CIR	Kairei[q]	3.0E+03	360	100					50
	JDFR	ASHES[r]	1.0E+04	280	50	9	21			55
	MAR	Lucky Strike[s]	6.4E+05	325	600	11	25	2.1E+07	3	22

[a]Integrated measurements refer to heat output measurements from water-column studies. Point measurements refer to heat output measurements at discrete vents and extrapolated to the vent field. Fields are left blank where data are not available.

[b]Vent field area is likely to be a maximum value incorporated the entire area over which venting occurs. Actual discharge is often focused within a significantly smaller area than listed here.

[c]These are average temperatures of black smoker venting.

[d]Heat output values are uncertain by ± a factor of 2.

[e]Magma chamber area is determined by the cross-axis width from reflection seismology and the length is estimated from the size and spacing of vent fields. The uncertainty in magma chamber cross section is ~ 10–20%.

[f]*German and Lin* [2004], *German et al.* [2010]. [g]*Murton et al.* [1995, 1999]. [h]*Baker* [2007], *Rona et al.* [1993], *Canales et al.* [2007]. [i]*Baker and Massoth* [1987], *Ginster et al.* [1994], *Canales et al.* [2005]. [j]*Baker* [2007], *Embley and Chadwick* [1994], *Canales et al.* [2005]. [k]*Delaney et al.* [1997], *Kelley et al.* [2002], *Thompson et al.* [2005], *Van Ark et al.* [2007]. [l]*Robigou et al.* [1993], *Thompson et al.* [2005], *Van Ark et al.* [2007]. [m]*Delaney et al.* [1992, 1997], *Kelley et al.* [2002], *Veirs et al.* [2006], *Van Ark et al.* [2007], *Baker* [2007]. [n]*Kelley et al.* [2001], *Thompson et al.* [2005], *Van Ark et al.* [2007]. [o]*Von Damm and Lilley* [2004], *Ramondenc et al.* [2006], *Tolstoy et al.* [2008], *Detrick et al.* [1987]. [p]*Macdonald et al.* [1980], *Spiess et al.* [1980], *Converse et al.* [1984]. [q]*Hashimoto et al.* [2001], *Rudnicki and German* [2002]. [r]*Rona and Trivett* [1992], *Lang et al.* [2006]. [s]*Barreyre et al.* [2012], *Singh et al.* [2006], *Cooper et al.* [2000], *Charlou et al.* [2000].

and a deep discharge zone through which the hydrothermal fluid vents to the seafloor [e.g., *Lowell and Germanovich*, 1994, 2004; *Lowell et al.*, 2008, 2012]. In this case observed values of T_d and H are used to determine Q, and observations of the vent field area A_d and planform area of the AMC A_m are used to determine the conductive boundary layer thickness δ and the bulk permeability of the discharge zone k_d. A cartoon showing the assumed flow path in the single-pass model, details of the mathematical formulation, and the definition of all symbols are given in Appendix A.

2.2. The Two-Limb Single-Pass Model

[6] At oceanic spreading centers, much of the thermal energy discharges as low-temperature diffuse flow [*Schultz et al.*, 1992; *Rona and Trivett*, 1992; *Baker et al.*, 1993; *Ramondenc et al.*, 2006]. To characterize partitioning of heat output in seafloor hydrothermal systems, a second limb is added to describe a shallow circulation cell within which seawater may be heated and mix with high-temperature fluid to produce low-temperature diffuse flow [e.g., *Pascoe and Cann*, 1995; *Lowell et al.*, 2003; *Ramondenc et al.*, 2008;

Lowell et al., 2012; *Bemis et al.*, 2012]. The depth of this mixing zone is not well defined, but is likely to be confined mainly to the seismic layer 2A [e.g., *Germanovich et al.*, 2011].

[7] In the two-limb single-pass model, we assume that as the ascending, sulfate-depleted, hot hydrothermal fluid mixes with the sulfate-rich, shallow recharge of cold seawater in the extrusive layer, anhydrite and other minerals precipitate, resulting in permeable channels of focused flow separated from regions of low-temperature diffuse flow [*Lowell et al.*, 2003, 2012; *Germanovich et al.*, 2011]. We also assume that there is no conductive cooling of the high-temperature fluid or mixing with seawater during its ascent. We denote the high-temperature and diffuse mass flow components exiting the seafloor by Q_3 and Q_4, respectively, whereas Q_1 refers to the mass flow in the deep recharge zone and Q_2 refers to the mass flow of the shallow recharge. We denote the mean temperature of high-temperature and diffuse vent fluids by T_3 and T_4, and the heat outputs by H_3 and H_4, respectively. To obtain the fraction of high-temperature fluid that is incorporated into the diffuse flow component, we use Mg concentration as a tracer. We assume that black smoker fluid is a 0

Mg end-member fluid that has not mixed with cold seawater and that the difference between the Mg concentration in the diffuse flow fluid and seawater reflects the incorporation of the 0 Mg end-member fluid. Appendix A provides details on the geometry of hydrothermal circulation and the mathematical formulation of the two-limb single-pass model.

[8] As we show in section 3.2.1, once we have determined the fraction of high-temperature fluid incorporated into the diffuse discharge, we can then use a simple energy balance to determine whether temperature can serve as a conservative tracer. We show that temperature is nearly conservative for the EPR 9°50′N and ASHES vent fields but not for MEF and Lucky Strike. We suggest that diffuse flow fluids appear to have cooled conductively at MEF and have been heated conductively at Lucky Strike. Finally, we use the two-limb single-pass model to estimate the chemical transport of various species in both diffuse and high-temperature discharge. This is particularly useful for chemical constituents such as H_2, CH_4, and CO_2 that may be affected by biogeochemical processes in the shallow crust. Chemical transport is discussed in section 3.2.2.

3. Results

3.1. Fundamental Vent-Field-Scale Characteristics

[9] Although approximately 1000 hydrothermal fields are predicted to exist along the global ridge system and approximately one third of these have been identified [Baker and German, 2004], the data

to constrain the fundamental parameters Q, k_d, and δ are limited to approximately 15 sites worldwide (Table 1). We use the observational constraints T_d, H, A_m, and A_d (Table 1) in the classical single-pass model formulation to obtain the results given in Table 2. Despite significant differences in spreading rate and depth to the AMC, Q, k_d, and δ generally lie in fairly narrow ranges (Table 2) and do not differ greatly from the predictions of a generic model [Lowell and Germanovich, 2004]. The results in Table 2 are subject to considerable uncertainty, as we discuss in section 4.1.

3.1.1. Magma Replenishment

[10] A key feature of the magma-hydrothermal model presented here is that for high-temperature venting and heat output to be maintained on decadal time-scales, the rate of heat extraction from the underlying magma must remain nearly constant so that δ remains thin [Lowell and Germanovich, 1994, 2004], but as heat is transferred from the convecting magma, the AMC is gradually crystallizing and cooling. Lowell et al. [2008] and Liu and Lowell [2009] showed that crystallization and cooling will result in relatively rapid decay in hydrothermal heat output and hydro-thermal temperature unless the magma chamber is actively undergoing replenishment from below.

[11] To determine the rate of magma replenishment, we equate the rate of hydrothermal heat output with the removal of latent heat from magma, along with some modest degree of cooling. If magma at its liquidus temperature T_L enters the magma chamber and cools to some temperature T_m greater than the

Table 2. Values of Q, k, δ, $\dot{V}_m$, and τ are Shown for Various Hydrothermal Vent Sites

	Site		Q^a (kg/s)	$k_d{}^b$ (m²)	δ^a (m)	$\dot{V}_m{}^a$ (m³/s)	τ^b (a)
Integrated measurements	MAR	Rainbow	275	4E−13		0.50	
		Broken Spur	15	1E−13		0.03	
		TAG	934	1E−12		1.70	4.99
	JDFR	Southern Cleft	110	4E−14	21	0.19	40.25
		Northern Cleft	340	2E−13	8	0.55	15.01
		Salty Dawg	32	2E−12		0.05	1.58
		High Rise	303	8E−14		0.50	25.78
		MEF	247	2E−13	5	0.45	12.42
		Mothra	73	8E−14		0.10	42.73
Point measurements	EPR	9°50′N	86	3E−13	13	0.16	3.86
		21°N	114	8E−13		0.20	
	CIR	Kairei	56	7E−13		0.10	
	JDFR	ASHES	36	2E−13		0.05	
	MAR	Lucky Strike	369	3E−14	73	0.60	110

[a]Mass flow values, boundary layer thickness, and magma replenishment rates are uncertain by about a factor of 2 because of the uncertainty in heat output. The values listed are rounded to whole numbers.
[b]Permeability values may be underestimated and residence times may be overestimated by about a factor of 10, respectively, because of the un-certainty in heat output and because the vent field area is an upper estimate.

solidus, the amount of heat H_m released upon cooling per unit volume of magma is

$$H_m = \rho_m c_m (T_L - T_m) + \rho_m \gamma L \qquad (1)$$

where ρ_m is the density, c_m is the specific heat, and L is the latent heat of the magma, respectively, and γ is the crystal content that develops as magma cools from T_L to T_m. Details of latent heat release and cooling of gabbroic magmas is somewhat complex [e.g., *Maclennan*, 2008], but it appears that most of the latent heat is released at $T_m > 1050°$, even though the solidus temperature may be as low as 860°C [*Coogan et al.*, 2001]. For simplicity, we assume that cooling over 100°C results in release of 50% of the latent heat.

[12] The parameters in Table A1 give $H_m = 10^9$ J/m^3. If magma is entering the base of the magma chamber through an area A_m at a constant velocity u_m, balancing the rate of heat input with high-temperature hydrothermal heat output is

$$u_m A_m H_m = \dot{V}_m H_m = H \qquad (2)$$

where $\dot{V}_m$ is the rate of magma replenishment (m^3/s). Equation (2) assumes that magma replenishment provides the total heat output of the hydrothermal system, whereas *Lowell* [2010] assumed that it provided only 50% of the total. The values of $\dot{V}_m$ shown in Table 2 are similar to those determined by *Liu and Lowell* [2009] and to that measured at Axial Volcano following the 1998 eruption [*Nooner and Chadwick*, 2009].

3.1.2. Thermal Anomaly Transport

[13] The mass flux Q from Table 2 and the vent field area A_d from Table 1 for representative sites provide an estimate for the Darcian velocity in the discharge zone. This value coupled with the depth to the AMC h (Table 1) provides an estimate of the time τ to transport a thermal anomaly from the AMC to the

seafloor [e.g., *Wilcock*, 2004; *Germanovich et al.*, 2011]. That is,

$$\tau = \frac{\rho_f h A_d}{Q} \qquad (3)$$

[14] The values in Table 2 indicate that fluid residence times range between a few years and several decades. The values determined from equation (3) are most strongly affected by the estimate of vent field area A_d. As discussed in section 4.1, these are likely to be overestimates because we assume that A_d corresponds to the mapped area of the vent field. Even if the residence times from equation (3) were reduced by a factor of 10, however, thermal perturbations near the top of the AMC would take months to reach the seafloor [e.g., *Germanovich et al.*, 2011]. Conductive cooling would tend to diminish the amplitude of such perturbations [*Wilcock*, 2004; *Ramondenc et al.*, 2008]. Temperature perturbations at the seafloor following seismic swarms at EPR 9°50′N have been observed in a matter of days, however [*Sohn et al.*, 1998; *Tolstoy et al.*, 2008]. Because of this discrepancy, *Germanovich et al.* [2011] argued that processes such as fluid mixing and thermal conduction in the shallow crust may control the thermal response time for such events.

3.2. Results From the Two-Limb Model

3.2.1. Comparison With the Classical Model

[15] Using the input data on mean discharge temperature along with heat output (Table 1) and the mixing fraction determined from Mg partitioning (Table A2), the governing equations of the two-limb model and chemical balances (see Appendix A) yield values of the mass fluxes Q_1 through Q_4 (Table 3). A comparison between Q_1 and Q, which comes from the classical single-pass model, shows that for ASHES and EPR 9°50′N, Q_1 is slightly smaller than Q, whereas for MEF and Lucky Strike, the differences are significant. For MEF, Q_1 is greater

Table 3. Mass Fluxes for the Two-Limb Model Compared with Q From the Classical Model[a]

Site	Results					Results			
	Mg Tracer					T Tracer			
	Q_1 (kg/s)	Q_2 (kg/s)	Q_3 (kg/s)	Q_4 (kg/s)	Q^b (kg/s)	Q_1 (kg/s)	Q_2 (kg/s)	Q_3 (kg/s)	Q_4 (kg/s)
EPR	80	1146	11	1207	86	81	1165	11	1236
MEF	292	1772	123	1940	247	241	1237	123	1355
ASHES	31	498	4	536	36	32	541	4	570
Lucky Strike	119	5412	31	5500	369	291	15978	31	16238

[a]Results use Mg and temperature as tracers.
[b]The value Q represents the mass flux from the vent field if all the heat output were at high temperature. Note that the results here are slightly different from those shown in *Lowell et al.* [2012] and *Bemis et al.* [2012] because of slightly different averaging.

than Q. This is a surprising result since heat flow partitioning between focused and diffuse sources should result in $Q_1 < Q$. For Lucky Strike, Q_1 is significantly smaller than Q.

[16] The close correspondence between Q_1 and Q for the EPR, ASHES, and MEF vent fields suggests that although most of the heat output leaves the crust as diffuse flow, 85%–90% of the heat output is ultimately a result of high-temperature magma-driven flow rather than a result of seawater circulating in the shallow crust. We discuss below the unexpected result that Q_1 appears to be greater than Q at MEF. For Lucky Strike, however, the value of Q_1 gives a high-temperature heat output of 229 MW compared to a total observed heat output of ~ 600 MW [*Barreyre et al.*, 2012].

[17] To better understand the results for MEF and Lucky Strike, we explore the use of temperature as a tracer. A simple thermal energy balance based on linear mixing between seawater and high-temperature fluid to result in diffuse flow discharge can be written as follows:

$$c_{ht}(Q_1 - Q_3)T_3 + c_{lt}Q_2T_2 = c_{lt}Q_4T_4 \qquad (4)$$

[18] Assuming a shallow recharge temperature $T_2 = 2°C$, using the Q values from Table 3 where we used Mg as a tracer, and observed values of T_3, we calculate the expected value of diffuse flow temperature T_4. The results in Figure 1 show that for EPR and ASHES, the diffuse flow temperatures calculated from equation (4) are nearly equal to the observed temperatures. This is consistent with the results in section 3.2 indicating that most of hydrothermal heat output results from high-temperature flow, even though a significant fraction of the heat

output discharges as low-temperature diffuse flow. We then recalculate Q_1, Q_2, and Q_4 using the new estimate of T_4 (Table 3). Q_3 remains the same. For MEF, the value of Q_1 for the two-limb system is now less than Q (Table 3) as expected. Equation (4) is in much closer balance with the new estimates of the various Q values and the calculated value for T_4. The average diffuse flow temperature should be $\approx 41°C$ rather than 29°C as observed, which suggests that the diffuse flow fluids at MEF have undergone substantial conductive cooling. With the new value of $Q_1 = 241$ kg/s (see Table 3), we estimate that $\sim 98\%$ of the heat output at MEF results from high-temperature fluid flow.

[19] In contrast, at Lucky Strike the observed diffuse flow temperature is 25°C, whereas the calculated value from equation (4) is approximately 8.5°C. This result indicates that the diffuse flow fluid has undergone considerable conductive heating, as argued by *Cooper et al.* [2000]. Using 8.5°C for the diffuse flow temperature in Table 1, we find $Q_1 = 291$ kg/s (Table 3), which is nearly 3 times the value determined by using the observed vent temperature. Then we estimate that nearly 80% of the advective heat output resulted from high-temperature fluid. This is still a smaller percentage than for the other systems, which indicates that a significant portion of the diffuse discharge at Lucky Strike stems from seawater that is heated during circulation in the shallow crust.

[20] The result that a large fraction of the hydrothermal heat output is diluted high-temperature fluid indicates that the Q, k_d, δ, $\dot{V}_m$, and τ values determined for the classical single-pass model in Table 2 are reasonable estimates, given the uncertainties in parameters H
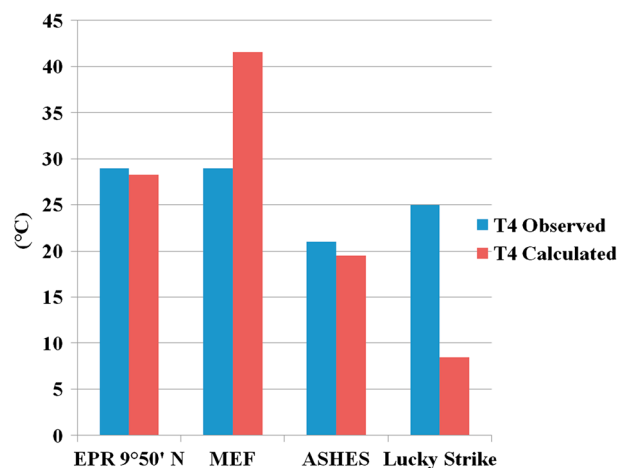

Figure 1. Comparison between observed mean diffuse flow temperature T_4 with that expected from mixing between seawater and high-temperature fluid.

and A_d. Thus, the classical single-pass model is a useful means of estimating key magma-hydrothermal parameters at the vent field scale and provides a useful starting point for constructing numerical models. Data on partitioning of heat output between focused and diffuse flow would not change the estimates of the parameters in Table 2 appreciably, but these data are important for understanding the nature of diffuse flow. As shown below, such data are also needed to understand geochemical transport, which in turn sheds light on biogeochemical processes.

3.2.2. Geochemical Transport at the Vent Field Scale

[21] Geochemical fluxes from seafloor hydrothermal systems are needed for understanding geochemical cycling between the ocean and lithosphere and for understanding the utilization of chemical constituents by microbial and macrofaunal communities [e.g., *Crowell et al.*, 2008; *Lang et al.*, 2006; *Wankel et al.*, 2011]. By using the two-limb single-pass model, the partitioning of geochemical transports between focused and diffuse flow can be determined. To determine geochemical transports F at the vent field scale for diffuse and focused flow, respectively, we multiply the observed concentration of a chemical constituent C for a given flow component by the respective mass flow Q. Thus, for high-temperature focused flow, $F_3 = C_3 Q_3$, whereas for low-temperature diffuse flow, $F_4 = C_4 Q_4$.

[22] This approach differs from that of *Lang et al.* [2006], who estimated flux of dissolved organic carbon (DOC) on the global scale, and *Wankel et al.* [2011], who determined geochemical fluxes of CH_4, CO_2, and H_2 at specific discharge sites on the Juan de Fuca Ridge. Taking the average concentration of

dissolved organic carbon in focused and diffuse vent sites on the MEF from *Lang et al.* [2006] and using $700\,kg/m^3$ as the density of high-temperature fluid, we obtain $C_3 \approx 21\,\mu mol/kg$ and $C_4 \approx 47\,\mu mol/kg$, respectively. Using the values Q_3 and Q_4 for MEF from Table 3, where we use flow values assuming that temperature is the tracer, we obtain a DOC flux $F_{DOC} = 2.6\,mmol/s$ from high-temperature vents and $F_{DOC} = 63\,mmol/s$ from diffuse vents. These results suggest that the dissolved organic carbon transport via diffuse flow is 24 times greater than that from high-temperature vents. Note that these estimates correct an error in *Bemis et al.* [2012], where we inadvertently used an incorrect mass flow to calculate the transport of DOC by diffuse flow.

[23] Similarly, we consider chemical transport along the Northern Transect at EPR 9°50′N, where the concentrations of a number of chemical species have been determined for both black smoker and diffuse discharge [*Von Damm and Lilley*, 2004]. Figure 2a shows that the chemical transport by diffuse flow ranges from approximately 3 to 6 times that from black smokers for all the elements except H_2. Figure 2a shows that a significant fraction of H_2S, Fe, and Mn transport at EPR occurs by diffuse flow.

[24] To determine whether CO_2, H_2, and CH_4 are used by subsurface microbes, we use a mixing relationship analogous to equation (4):

$$C_4 Q_4 = C_3(Q_1 - Q_3) + C_2 Q_2 \tag{5}$$

[25] The mean concentration data are calculated from Table 2 of *Von Damm and Lilley* [2004]. Figure 2b shows the results. By comparing the expected concentration for CO_2, H_2, and CH_4 based on simple mixing, we find that the observed concentrations are less than that derived from equation (5). This implies that each of these components is being utilized
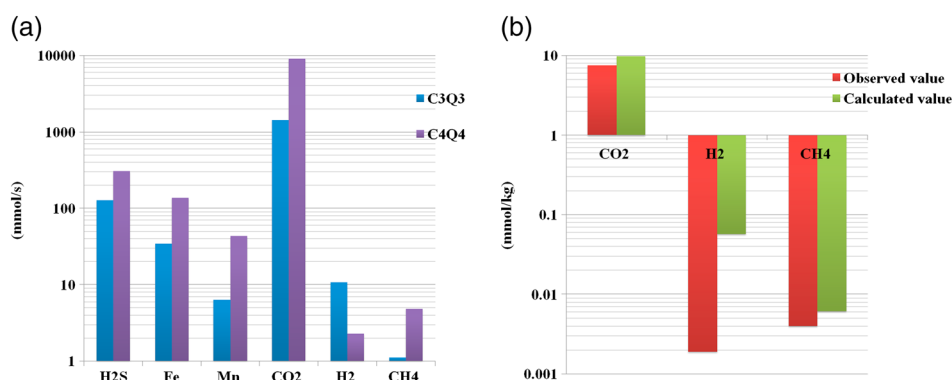

Figure 2. (a) Mean transport rate for several chemical species in focused (C_3Q_3) and diffuse flow (C_4Q_4) from EPR 9°50′N. Average values of C_3 and C_4 are calculated from Table 2 of *Von Damm and Lilley* [2004]; values of Q_3 and Q_4 are taken from Table 3, using temperature as a tracer. (b) Comparison between measured values of CO_2, H_2, and CH_4 in diffuse flow fluids from EPR 9°50′N with values calculated assuming simple mixing.

by subsurface microbes. H_2 is depleted by approximately 97%, whereas CH_4 and CO_2 are depleted by approximately 35% and 23%, respectively.

4. Discussion

4.1. Model Robustness and Uncertainties

[26] Amongst observational data, temperature has the least amount of uncertainty, whereas heat output and area of discharge are the largest sources of uncertainty in modeling.

[27] In general, vent fluid temperature and chemistry, particularly of high-temperature vents, are routinely measured, and the vent field area is mapped. Heat output data and seismic mapping of the AMC are relatively scarce, however, and as a result, all of these key data characteristics are known for fewer than ten hydrothermal sites (Table 1). At present, heat output data have a high level of uncertainty, which limits the ability to interpret mass flows and geochemical transports from the vent field. Despite this uncertainty heat output is critically important for characterizing the hydrothermal system. Thus, we argue that determination of heat output and its partitioning between focused and diffuse flow should become a routine exercise in hydrothermal investigations.

[28] Vent field area is needed to estimate crustal permeability and fluid residence time. We use the area of the vent field found from detailed mapping, but this area is likely to be an overestimate of the area of the hydrothermal discharge zone and hence is not entirely representative of the subsurface

plumbing system and hydrologic flow paths. Typically hydrothermal discharge of both high-temperature vent chimneys and diffuse flow areas are localized within the broad area that defines the vent field. At EPR 9°50′N, detailed seafloor mapping by *Ferrini et al.* [2007] suggests that focused venting and adjacent diffuse flow patches may occupy ~ $10^3 \, m^2$, which is an order of magnitude smaller than the mapped vent field area. The active high-temperature vent structures in the MEF are localized along faults and appear to occupy ~ 10%–20% of the vent field area. At Lucky Strike, venting is localized along faults surrounding the lava lake [*Barreyre et al.*, 2012]. These observations suggest that hydrothermal discharge is focused through high-permeability features within the vent field area. Diffuse flow is more broadly distributed than the discrete high-temperature discharge [e.g., *Barreyre et al.*, 2012], and since diffuse flow is a mixture of seawater and high-temperature fluid, upwelling high-temperature discharge is not restricted to discrete chimneys and high-temperature vent structures. More realistic estimates of crustal permeability and fluid residence times require a better understanding of the subsurface plumbing system. Permeability and effective vent field area are likely to be highly heterogeneous. The estimates of bulk permeability given in Table 2 may underestimate the effective permeability by an order of magnitude, and residence times may be overestimated by a similar amount.

4.2. Hydrothermal Heat Flux, Spreading Rate, and Depth to the AMC

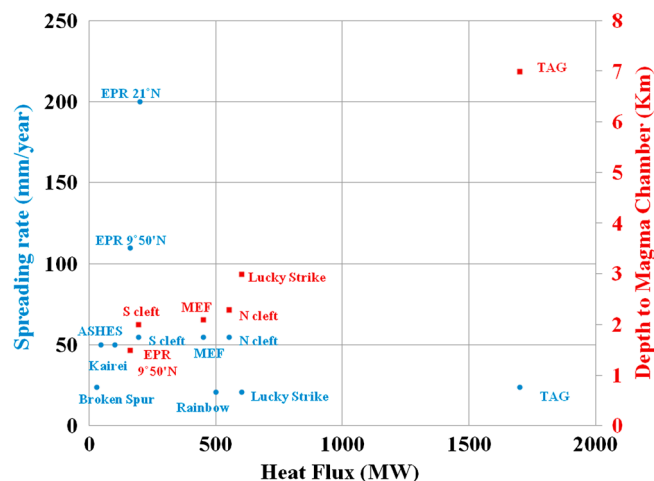[29] *Baker and German* [2004] have shown a strong correlation globally between hydrothermal venting

Figure 3. Data showing relationship between depth to AMC, spreading rate, and heat output for hydrothermal sites at oceanic spreading centers. The available data are taken from Table 1.

frequency and magma supply, or spreading rate. *Baker* [2009] further suggested that at intermediate-through fast-spreading rates at the multisegment scale ridge length, plume incidence increases as the depth to the AMC decreases. This correlation weakens at the second-order segment scale though, and the data are scarce for slow-spreading ridges. *Baker* [2009] argued that high-temperature hydrothermal venting is closely linked to the presence of subsurface magma in all spreading environments. Here we explore two other correlations using the limited heat flux data from the vent sites in Table 1.

[30] Figure 3 shows spreading rate and magma chamber depth versus mean estimates of vent field heat flux. The plot of heat output versus spreading rate shows essentially no correlation between spreading rate and heat output. In fact, the highest heat outputs often appear to be found at slow-spreading ridges (i.e., Rainbow, Lucky Strike, and TAG). Since heat output may be viewed as a proxy for magma supply [*Baker and German*, 2004], we interpret this lack of correlation to be an indication that hydrothermal heat output at active hydrothermal systems is not a function of magma supply in a "time-integrated" sense corresponding to spreading rate. Rather, it is a function of magma supply on a local spatial and temporal scale. This is a slightly different way of stressing the importance of magma supply as a driver of high-temperature hydrothermal venting at all spreading rates. This may also explain why black smokers do not exist everywhere above mapped AMCs.

[31] Figure 3 also shows no obvious correlation between heat output and depth of the magma chamber. This lack of correlation suggests that if magma is present, regardless of depth, crustal permeability tends to evolve in such a manner as to tap the available heat. It also suggests, qualitatively at least, that hydrothermal circulation simply takes the heat supplied by the convecting magma body. It does not extract heat from the crustal rocks or suppress magmatic heat output by cooling the overlying crust. This argument is somewhat counter to that of *Morgan and Chen* [1993], who argued that hydrothermal cooling near the ridge axis, which is proportional to the spreading rate, controls the depth of the AMC. The difference between these two approaches is that *Morgan and Chen* [1993] considered a time-integrated scale related to crustal spreading, whereas we consider a timescale related to a local rate of magma supply and the lifetime of a hydrothermal field, which may be only tens to hundreds of years. *Mittelstaedt et al.*, 2012 provided additional discussion of the connections between hydrothermal heat output, depth to the AMC, and spreading rate.

5. Conclusions

[32] We use one- and two-limb single-pass hydrothermal models to provide estimates of key hydrothermal characteristics such as bulk permeability, mass flow rate, conductive boundary layer thickness, magma replenishment rate, and fluid residence time. The models are constrained by observational data on vent temperature, heat output, vent field area, and surface area and depth of the subaxial magma chamber. The principal limitations of this approach stem from lack of heat output and magma chamber data, which are available for only a small fraction of the more than 300 known systems. The uncertainty in these estimates primarily reflects uncertainty in hydrothermal heat output and area of the vent field. Vent field areas used in these simple models are likely overestimates, which translates into underestimates of crustal permeability and overestimates of fluid residence time in the discharge zone, respectively. Despite these uncertainties, it is noteworthy that Q, k_d, and δ tend to cluster over similar ranges of $\sim 100 \, \text{kg/s}$, $\sim 10^{-13} \, \text{m}^2$, and $\sim 10 \, \text{m}$, respectively, suggesting that the single-pass model provides reasonable first-order estimates of key hydrothermal characteristics independent of spreading rate and detailed information about the AMC.

[33] Using data on heat output, vent temperature, and Mg concentration for focused and diffuse flow in a two-limb model, we can obtain useful constraints on the fraction of high-temperature fluid incorporated into diffuse flow. If geochemical data are available, the model also yields estimates of geochemical transports in focused and diffuse flows, respectively, and whether microbial processes act as sources or sinks for certain chemical constituents such as CO_2, H_2, and CH_4. Our calculations for EPR 9°50′N suggest that all of these constituents are removed by microbial processes in regions of diffuse flow. The results of the two-limb model indicates that typically 80%–90% of the hydrothermal heat output occurs as high-temperature flow derived from magmatic heat even though most of the heat output discharges as low-temperature diffuse discharge. By comparing calculated flow rates using Mg and vent fluid temperature as conservative tracers, we argue that EPR 9°50′N and ASHES diffuse flow fluids are

conservative mixtures, whereas MEF fluids have undergone conductive cooling and Lucky Strike fluids have undergone considerable conductive heating.

[34] There is no apparent correlation between heat output or depth to the magma chamber and spreading rate. These results suggest that heat output from individual seafloor hydrothermal systems is controlled by local, short-lived magma supply rates rather than by the long-term magma supply needed for crustal production and that crustal permeability evolves in such a manner to enable hydrothermal flow to tap the available heat supply regardless of its depth.

[35] Lack of data on hydrothermal heat output, subsurface plumbing and fluid flow patterns, and AMC characteristics limits our ability to model and understand magma-driven seafloor hydrothermal systems in more detail.

Appendix A:

A1. The Classical Single-Pass Model

[36] In the single-pass model (Figure A1), conservation of mass is expressed simply as Q, the mass flow
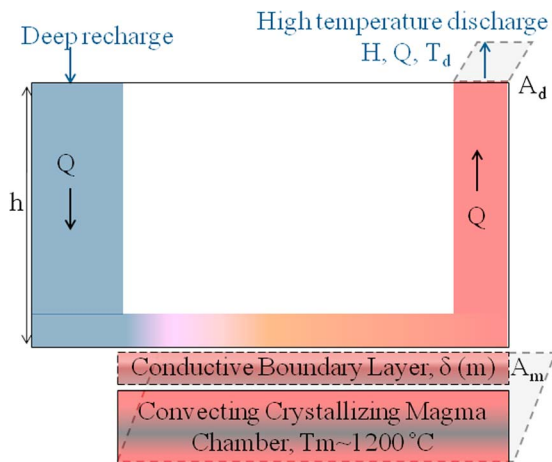

Figure A1. A schematic of the classical single-pass model. Cold seawater percolates downward to near the top of the subaxial magma chamber, which is maintained at a constant temperature $T_m \sim 1200°C$. Heat from the magma over an area A_m is transported to the hydrothermal system across a conductive boundary layer of thickness δ in the horizontal limb, where high-temperature water-rock reactions and phase separation occur. The hot buoyant hydrothermal fluid then ascends to the seafloor where it exits at a temperature T_d and mass flow rate Q through a vent field of area A_d. The heat output of the hydrothermal system is H. Modified from *Lowell et al.* [2008] and *Liu and Lowell* [2009].

rate (kg/s) through the single-pass circulation pathway. Conservation of momentum is expressed by an integrated form of Darcy's law, which is equivalent to Ohm's law for an electric circuit. For buoyancy-driven flow this is given by [e.g., *Lowell and Germanovich*, 2004]

$$Q = \frac{\widehat{H}}{R} = \frac{\rho_{f0}g\int_0^h \alpha(z)[T_d(z) - T_r(z)dz]}{\int_0^{L*} \frac{v}{kA}ds} \quad (A1)$$

where $\widehat{H}$ is the buoyancy driving the flow, and R is the integrated flow resistance along the circulation path. In equation (A1), ρ_{f0} is the fluid density at $0°C$, g is the acceleration due to gravity, α is the thermal expansion coefficient, T is the temperature, v is the kinematic viscosity of the fluid, k is the permeability, A is the cross-sectional area through which the fluid passes, h is the height of the circulation layer, and $L*$ is the total length of the flow path. The subscripts d and r refer to the discharge and recharge zones, respectively. All symbols are listed in Table A1. If we assume that $T_r = 0$ and $T_d(z) = T_d$ (a constant representing the vent fluid temperature) and that the flow resistance occurs primarily in the discharge zone, equation (A1) can be simplified to

$$Q = \frac{\rho_{f0}\alpha_d g k_d T_d A_d}{v_d} \quad (A2)$$

[37] Conservation of energy is expressed as a simple heat balance between the heat conducted across the thermal boundary layer δ and the advective heat flux out of the system. That is,

$$\frac{\lambda(T_m - T_d/2)A_m}{\delta} = c_{ht}QT_d = H \quad (A3)$$

where λ is the thermal conductivity of the rock, T_m is the temperature of the magma, A_m is the area of the AMC from which heat is transferred to the hydrothermal system, c_{ht} is the specific heat of the high-temperature venting fluid, and H is the total observed heat output of the hydrothermal system.

A2. Two-Limb Single-Pass Model

[38] In the two-limb model, the mass flux Q_1 at temperature T_1 in the deep recharge zone enters the cross-flow channel where heat transferred from the AMC raises the temperature from T_1 to T_3
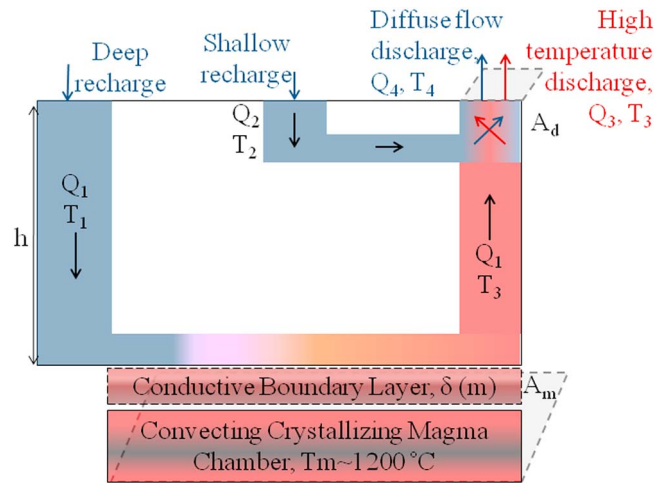
Figure A2. Schematic of a "double-loop" single-pass model above a convecting, crystallizing, replenished AMC (not to scale). Heat transfer from the vigorously convecting, cooling, and replenished AMC across the conductive boundary layer δ drives the overlying hydrothermal system. The deep circulation represented by mass flux Q_1 and black smoker temperature T_3 induces shallow circulation noted by Q_2. Some black smoker fluid mixes with seawater resulting in diffuse discharge Q_4, T_4, while the direct black smoker mass flux with temperature T_3 is reduced from Q_1 to Q_3. Heat output, vent temperature, and geochemical data allow estimates of the various mass fluxes. Modified from *Germanovich et al.* [2011] and *Farough* [2012].

(Figure A2) in the discharge zone. The ascending mass flux Q_1 is then divided into two parts. One part, corresponding to Q_3, vents at the surface at temperature T_3, giving rise to the black smoker heat flux H_3. The remainder, Q_1–Q_3, mixes with cold seawater in the shallow limb that has mass flux Q_2 and arrives at the seafloor as diffuse flow Q_4 with a diffuse flow temperature T_4 and a resultant diffuse flow heat flux H_4. The mass fluxes Q_3 and Q_4 can be determined directly from the heat flux and temperature data and specific heat using the following formulas [e.g., *Lowell et al.*, 2012]:

$$Q_3 = \frac{H_3}{c_{ht}T_3}; \qquad Q_4 = \frac{H_4}{c_{lt}T_4} \qquad (A4)$$

where c_{ht} and c_{lt} are the specific heat of the fluid at high and low temperatures, respectively.

[39] We then use Mg concentration as a conservative tracer to obtain the fraction ξ of the black smoker fluid entrained in the diffuse flow. We assume that the black smoker fluid is an end-member hydrothermal fluid with Mg = 0. Writing the Mg concentration χ, we have

$$\xi = \frac{X_{lt} - X_{sw}}{X_{ht} - X_{sw}} = \frac{Q_1 - Q_3}{Q_4} \qquad (A5)$$

where the subscripts *lt*, *ht*, and *sw* refer to diffuse, high-temperature, and seawater concentrations, respectively. Since Q_3 and Q_4 can be determined

from the heat output data and ξ can be determined from geochemical data on Mg in seawater and diffuse flow, the mass flux Q_1 can be determined from equation (A2). Finally, the shallow recharge Q_2 can be found from conservation of mass. That is,

$$Q_2 = Q_4 - (Q_1 - Q_3) \qquad (A6)$$

References

Baker, E. T. (2007), Hydrothermal cooling of mid ocean ridge axes: Do measured and modeled heat fluxes agree?, *Earth Planet. Sci. Lett.*, *263*, 140–150.

Baker, E. T. (2009), Relationships between hydrothermal activity and axial magma chamber distribution, depth, and melt content, *Geochem. Geophys. Geosyst.*, *10*(6), doi:10.1029/2009GC002424.

Baker, E. T., and C. R. German (2004), On the global distribution of hydrothermal vent fields, in Mid-Ocean Ridges: Hydrothermal Interactions Between the Lithosphere and Oceans, Geophys. Monogr. Ser., vol. 148, edited by C. R. German, J. Lin, and L. M. Parson, 318 pp., AGU, Washington, D. C., doi:10.1029/GM148.

Table A1.   List of Parameters Used in the Equations, Their Definition, Values in Both High Temperature and Low Temperature Diffuse Flow, and Their Units

Symbol	Definition	Value	Units
A	Cross-sectional area through which the fluid passes		m^2
A_d	Vent field discharge area		m^2
A_m	Area of the subaxial magma chamber over which heat is transferred to the hydrothermal system		m^2
C_m	Specific heat of magma	1400	J/kg °C
$c_{ht,\,lt}$	Specific heat of the fluid at high temperature and diffuse discharge	5000, 4000	J/kg °C
$C_{2,\,3,\,4}$	Concentration of chemical constituent in shallow recharge, high-temperature discharge, and diffuse discharge, respectively		mmol/kg
$F_{3,4}$	Geochemical transport rate in high-temperature and diffuse flow, respectively		mmol/s
G	Acceleration due to gravity	9.8	m/s^2
H	Depth to top of AMC		km
$\widehat{H}$	Buoyancy head driving the flow		
H	Total observed heat output of the hydrothermal system		W
$H_{3,\,4}$	Heat output of high-temperature and diffuse flow, respectively		W
H_m	Heat released upon cooling per unit volume of magma	10^9	J/m^3
K	Permeability		m^2
k_d	Permeability of discharge		m^2
L^*	Total length of the flow path in single pass model		M
L	Latent heat of magma		J/kg
Q	Total mass flux in single-pass model		kg/s
$Q_{1,\,2,\,3,\,4}$	Mass flow rate in the deep recharge zone, shallow recharge, high-temperature discharge, and diffuse discharge zone, respectively		kg/s
R	Integrated flow resistance along the circulation path		
$T_{1,\,2,\,3,\,4}$	Temperature in the deep recharge zone, shallow recharge, deep discharge, and diffuse discharge zone, respectively		°C
T_d	Temperature of discharge in the single-pass model		°C
T_L	Basalt liquidus temperature	1200	°C
T_m	Mean magma temperature		°C
T_r	Recharge temperature in the single-pass model	0	°C
u_m	Magma replenishment velocity		m/s
V_m	Volumetric rate of magma replenishment		m^3/s
Z	Vertical Cartesian coordinate		M
α	Thermal expansion coefficient		1/°C
α_d	Thermal expansion coefficient of discharge	0.001	1/°C
γ	Crystal content of magma		
Δ	Conductive thermal boundary layer thickness		M
Λ	Thermal conductivity of the rock	2	W/m-°C
v	Kinematic viscosity of fluid		m^2/s
v_d	Kinematic viscosity of the fluid in the discharge zone		m^2/s
ξ	Mixing fraction of black smoker fluid entrained in the diffuse flow		
$\rho_{f0},\,\rho_f$	Density of the fluid at 0°C and at high temperature, respectively	1000, 700	kg/m^3
ρ_m	Density of magma	2900	kg/m^3
τ	Residence time for fluid in discharge zone		A
$\chi_{lt,ht,sw}$	Concentration of a passive tracer in diffuse flow, focused flow, and seawater, respectively		mmol/kg

Baker, E. T., and G. J. Massoth (1987), Characteristics of hydrothermal plumes from two vent fields on the Juan de Fuca Ridge, northeast Pacific Ocean, *Earth Planet. Sci. Lett.*, *85*, 59–73.

Baker, E. T., G. J. Massoth, S. L. Walker, and R. W. Embley (1993), A method for quantitatively estimating diffuse and discrete hydrothermal discharge, *Earth Planet. Sci. Lett.*, *118*, 235–249.

Barreyre, T., J. Escartín, R. Garcia, M. Cannat, E. Mittelstaedt, and R. Prados (2012), Structure, temporal evolution, and heat flux estimates from the Lucky Strike deep-sea hydrothermal field derived from seafloor image mosaics, *Geochem. Geophys. Geosyst.*, *13*, Q04007, 29 pp., doi:10.1029/2011GC003990.

Bemis, K., R. P. Lowell, and A. Farough (2012), Diffuse flow on and around hydrothermal vents at mid-ocean ridges, *Oceanography*, *25*(1), 182–191, doi:10.5670/oceanog.2012.16.

Canales, J. P., R. S. Detrick, S. M. Carbotte, G. M. Kent, J. B. Diebold, A. Harding, J. Babcock, M. R. Nedimović, and E. Van Ark (2005), Upper crustal structure and axial topography at intermediate spreading ridges: Seismic constraints from the southern Juan de Fuca Ridge, *J. Geophys. Res.*, *110*, B12104, doi:10.1029/2005JB003630.

Canales, J. P., R. Reves-Sohn, and B. J. deMartin (2007), Crustal structure of the Trans-Atlantic Geotraverse (TAG) segment (Mid-Atlantic Ridge, 26°10′N): Implications for the nature of hydrothermal circulation and detachment

Table A2. Diffuse Flow Temperature and Geochemical Data Collected at Axial, MEF, EPR 9°50′N, and Lucky Strike Hydrothermal (Modified From *Farough* [2012])

Location	Temperature (°C)	Mg (mmol/kg)	Average Temperature (°C)	Average Mg (mmol/kg)	ξ
Diffuse Samples: ASHES (2003)[a]					
Crack	35.3	49.3	21.43	50.30	0.051
Gollum	16	51.7			
Styx	13	49.9			
Diffuse Samples: MEF[a]					
S&M, MT2	8.7	51.9	28.98	48.37	0.087
Hulk	17.5	50.4			
Easter Island	23.6	48.75			
Dudley	74.1	41.8			
South Grotto	21	49			
Seawater	2	53			
Diffuse Samples: EPR 9° 50′N[b]					
B9 (1991)	22	49.7	28.79	49.2	0.057
BM9R, BM9lo, and BM12	30.9	49.6			
(1992, 1993, 1994, 1995, 1997, 2000)	29.9	50.4			
	32.3	48.1			
	33.3	46.3			
	27.2	50.5			
	25.9	49.8			
Seawater	1.8	52.2			
Diffuse Samples: Lucky Strike[c]					
F21-M0	34.3	52.5	25.12	52.07	0.016
F21-M1	130.6	51.7			
F21-M2	7.9	52.2			
F21-M3	20	52.2			
F21-M4	13.2	48.8			
F21-M5	21.9	52.3			
F23-M0	13.5	52.1			
F23-M1	15.4	52.4			
F23-M2	10.3	52.9			
F23-M3	19.2	49.4			
F23-M4	9.8	52.2			
F23-M5	8.1	52.6			
F25-M0	15.9	51.9			
F25-MI	21.1	52.8			
F25-M2	16.7	52.8			
F25-M3	20.8	52.9			
F25-M4	58.8	52.8			
F25-M5	14.7	52.8			
Seawater	2	52.9			

[a]*Lang et al.* [2006]. [b]*Von Damm and Lilley* [2004]. [c]*Cooper et al.* [2000].

faulting at slow spreading ridges, *Geochem. Geophys. Geosyst. 8*, Q08004, doi:10.1029/2007GC001629.

Charlou, J. L., J. P. Donval, E. Douville, P. Jean-Baptiste, J. Radford-Knoery, Y. Fouquet, A. Dapoigny, and M. Stievenard (2000), Compared geochemical signatures and the evolution of Menez Gwen (37°50′N) and Lucky Strike (37°17 ′N) hydrothermal fluids, south of the Azores Triple Junction on the Mid-Atlantic Ridge, *Chem. Geol.*, *171*, 49–75, doi:10.1016/S0009-2541(00)00244-8.

Converse, D. R., H. D. Holland, and J. M. Edmond (1984), Flow rates in the axial hot springs of the East Pacific Rise (21°N): Implications for the heat budget and the formation of massive sulfide deposits, *Earth Planet. Sci. Lett.*, *69*, 159–175.

Coogan, L. A., C. J. MacLeod, H. J. B. Dick, S. J. Edwards, A. Kvassnes, J. H. Natland, P. T. Robinson, G. Thompson, and M. J. O'Hara (2001), Whole-rock geochemistry of gabbros from the Southwest Indian Ridge: Constraints on geochemical fractionations between the upper and lower oceanic crust and magma chamber processes at (very) slow-spreading ridges, *Chem. Geol.*, *178*, 1–22, doi:10.1016/S0009-2541(00)00424-1, ISSN:0009-2541.

Cooper, M. J., H. Elderfield, and A. Schultz (2000), Diffuse hydrothermal fluids from Lucky Strike hydrothermal vent field: Evidence for a shallow conductively heated system, *J. Geophys. Res.*, *105*(B8), 19,369–19,375, doi:10.1029/2000JB900138.

Crowell, B. W., R. P. Lowell, and K. L. Von Damm (2008), A model for the production of sulfur floc and "snowblower" events at mid-ocean ridges, *Geochem. Geophys. Geosyst.*, *9*, Q10T02, doi:10.1029/2008GC002103.

Delaney, J. R., D. S. Kelley, M. D. Lilley, D. A. Butterfield, and R. E. McDuff (1997), The Endeavour Hydrothermal System I: Cellular circulation above an active cracking front yields large sulfide structures, "fresh" vent water, and hyperthermophilic archae, *RIDGE Events*, 8, 11–19.

Delaney, J. R., V. Robigou, R. E. McDuff, and M. K. Tivey (1992), Geology of a vigorous hydrothermal system on the Endeavor segment, Juan de Fuca Ridge, *J. Geophys. Res.*, 97, 19,663–19,682.

Detrick, R. S., P. Buhl, E. Vera, J. Mutter, J. Orcutt, J. Madsen, and T. Brocher (1987), Multi-channel seismic imaging of a crustal magma chamber along the East Pacific Rise, *Nature*, 326, 35–41.

Elder, J. W. (1981), Geothermal Systems, 508 pp., Academic, San Diego, Calif.

Elderfield, H., and A. Schultz (1996), Mid-ocean ridge hydrothermal fluxes and the chemical composition of the ocean, *Annu. Rev. Earth Planet. Sci.*, 24, 191–224.

Embley, R. W., and W. W. Chadwick Jr. (1994), Volcanic and hydrothermal processes associated with a recent phase of seafloor spreading at the northern Cleft segment: Juan de Fuca Ridge, *J. Geophys. Res.*, 99, 4741–4760, doi:10.1029/93JB02038.

Farough, A. (2012), A parameterized approach to partitioning between focused and diffuse heat output and modeling hydrothermal recharge at the East Pacific Rise 9°50′N, M.S. thesis, 79 pp, Virginia Tech, Blacksburg.

Ferrini, V. L., D. J. Fornari, T. M. Shank, J. C. Kinsey, M. A. Tivey, J. A. Soule, S. M. Carbotte, L. L. Whitcomb, D. Yoerger, and J. Howland (2007), Sub-meter bathymetric mapping of volcanic and hydrothermal features on the East Pacific Rise crest 9°50′N, *Geochem. Geophys. Geosyst.*, 8, Q01006, doi:10.1029/2006GC001333.

German, C. R., and J. Lin (2004), The thermal structure of the oceanic crust, ridge-spreading and hydrothermal circulation: How well do we understand their inter-connections?, in Mid-Ocean Ridges: Hydrothermal Interactions Between the Lithosphere and Oceans, Geophys. Monogr. Ser., vol. 148, edited by C. R. German, J. Lin, and L. M. Parson, 318 pp., AGU, Washington, D. C., doi:10.1029/GM148.

German, C. R., A. M. Thurnherr, J. Knoery, J.-L. Charlou, P. Jean-Baptiste, and H. N. Edmonds (2010), Heat, volume and chemical fluxes from submarine venting: A synthesis of results from the Rainbow hydrothermal field, 36°N MAR, *Deep Sea Res. Pt. 1*, 57, 518–527, doi:10.1016/j.dsr.2009.12.011.

Germanovich, L. N., R. P. Lowell, and P. Ramondenc (2011), Magmatic origin of hydrothermal response to earthquake swarms: Constraints from heat flow and geochemical data at 9°50′N, East Pacific Rise, *J. Geophys. Res.*, 116, B05103, doi:10.1029/2009JB006588.

Ginster, U., M. J. Mottl, and R. P. Von Herzen (1994), Heat flux from black smokers on the Endeavour and Cleft segments, Juan de Fuca Ridge, *J. Geophys. Res.*, 99, 4937–4950,

Hashimoto, J., S. Ohta, T. Gamo, H. Chiba, T. Yamaguchi, S. Tsuchida, T. Okudaira, H. Watabe, T. Yamanaka, and M. Kitazawa (2001), First hydrothermal vent communities from the Indian Ocean discovered, *Zoolog. Sci.*, 18(5), 717–721, doi:10.2108/zsj.18.717.

Kelley, D. S., J. A. Baross, and J. R. Delaney (2002), Volcanoes, fluids and life at mid-ocean ridge spreading centers, *Annu. Rev. Earth Planet. Sci.*, 30, 385–491.

Kelley, D. S., J. R. Delaney, and D. A. Yoerger (2001), Geology and venting characteristics of the Mothra Hydrothermal Field, Endeavour Segment, Juan de Fuca Ridge, *Geology*, 29, 959–962.

Lang, S. Q., D. A. Butterfield, M. D. Lilley, H. P. Johnson, and J. I. Hedges (2006), Dissolved organic carbon in ridge-axis and ridge-flank hydrothermal systems, *Geochim. Cosmochim. Acta*, 70, 3830–3842.

Liu, L., and R. P. Lowell (2009), Models of hydrothermal heat output from a convecting, crystallizing, replenished magma chamber beneath an oceanic spreading center, *J. Geophys. Res.*, 114, B02102, doi:10.1029/2008JB005846.

Lowell, R. P. (2010), Hydrothermal systems at slow-spreading ridges: Analysis of heat sources and heat transfer processes, in Diversity of Hydrothermal Systems on Slow Spreading Ridges, Geophys. Monogr. Ser., vol. 188, edited by P. A. Rona, C. Devey, J. Dyment, and B. Murton, pp. 11–26, AGU, Washington, D.C., doi:10.1029/2008GM000758.

Lowell, R. P., and L. N. Germanovich (2004), Seafloor hydrothermal processes: Results from scale analysis and single-pass models, in *Mid-Ocean Ridges: Hydrothermal Interactions Between the Lithosphere and Oceans, Geophys. Monogr. Ser.*, vol. 148, edited by C. R. German, J. Lin, and L. M. Parson, pp. 219–244, AGU, Washington, D. C.

Lowell, R. P., B. W. Crowell, K. C. Lewis, and L. Liu (2008), Modeling multiphase, multicomponent processes at oceanic spreading centers, in Magma to Microbe: Modeling Hydrothermal Processes at Ocean Spreading Centers, Geophys. Monogr. Ser., vol. 178, edited by R. P. Lowell, J. S. Seewald, A. Metaxas, and M. R. Perfit, 285 pp., AGU, Washington, D. C., doi:10.1029/GM178.

Lowell, R. P., A. Farough, L. N. Germanovich, L. B. Hebert, and R. Horne (2012), A vent-field-scale model of the East Pacific Rise 9°50′N magma-hydrothermal system, *Oceanography*, 25(1), 158–167, doi:10.5670/oceanog.2012.13.

Lowell, R. P., and L. N. Germanovich (2004), Hydrothermal processes at mid-ocean ridges: Results from scale analysis and single-pass models, in Mid-Ocean Ridges: Hydrothermal Interactions Between the Lithosphere and Oceans, Geophys. Monogr. Ser., vol. 148, edited by C. R. German, J. Lin, and L. M. Parson, 318 pp., AGU, Washington, D. C., doi:10.1029/GM148.

Lowell, R. P., Y. Yao, and L. N. Germanovich (2003), Anhydrite precipitation and the relationship between focused and diffuse flow in seafloor hydrothermal systems, *J. Geophys. Res.*, 108(B9), 2424, doi:10.1029/2002JB002371.

Macdonald, K. C., K. Becker, F. N. Spiess, and R. D. Ballard (1980), Hydrothermal heat flux of the "black smoker" vents on the East Pacific, *Earth Planet. Sci. Lett.*, 48, 1–7.

Maclennan, J. (2008), The supply of heat to mid-ocean ridges by crystallization and cooling of mantle melts, in Magma to Microbe: Modeling Hydrothermal Processes at Ocean Spreading Centers, Geophys. Monogr. Ser., vol. 178, edited by R. P. Lowell, J. S. Seewald, A. Metaxas, and M. R. Perfit, 285 pp., AGU, Washington, D. C., doi:10.1029/GM178.

Mittelstaedt, E., J. Escartin, N. Gracias, J.-A. Olive, T. Barreyre, A. Davaille, M. Cannat, and R. Garcia (2012), Quantifying diffuse and discrete venting at the Tour Eiffel vent site, Lucky Strike hydrothermal field, *Geochem. Geophys. Geosyst.*, 13, Q04008, doi:10.1029/2011GC003991.

Morgan, J. P., and Y. J. Chen (1993), The genesis of oceanic crust: Magma injection, hydrothermal circulation, and crustal flow, *J. Geophys. Res.*, 98, 6283–6297.

Murton, B. J., L. J. Redbourn, C. R. German, and E. T. Baker (1999), Sources and fluxes of hydrothermal heat, chemicals and biology within a segment of the Mid-Atlantic Ridge, *Earth Planet. Sci. Lett.*, 171, 301–317.

Murton, B. J., C. Van Dover, and E. Southward (1995), Geological setting and ecology of the Broken Spur hydrothermal vent field: 29°10′N, in Hydrothermal Vents and

Processes, edited by C. L. W. L. M. Parson and D. R. Dixon, pp. 33–41, The Geological Society of London, London.

Nooner, S. L., and W. W. Chadwick (2009), Volcanic inflation measured in the caldera of Axial Seamount: Implications for magma supply and future eruptions, *Geochem. Geophys. Geosyst.*, *10*, Q02002, doi:10.1029/2008GC002315.

Pascoe, A. R., and J. R. Cann (1995), Modeling diffuse hydrothermal flow in black smoker vent fields, in Hydrothermal Vents and Processes, edited by C. L. W. L. M. Parson and D. R. Dixon, pp. 159–173, The Geological Society of London, London.

Ramondenc, P., L. N. Germanovich, K. L. Von Damm, and R. P. Lowell (2006), The first measurements of hydrothermal heat output at 9°50′N, East Pacific Rise, *Earth Planet. Sci. Lett.*, *245*, 487–497, doi:10.1016/j.epsl.2006.03.023, ISSN:0012-821X.

Ramondenc, P., L. N. Germanovich, and R. P. Lowell (2008), Modeling the hydrothermal response to earthquakes at oceanic spreading centers, in Magma to Microbe: Modeling Hydrothermal Processes at Ocean Spreading Centers, Geophys. Monogr. Ser., vol. 178, edited by R. P. Lowell, Seewald J. S., Metaxas A., Perfit M. R., 285 pp., AGU, Washington, D. C., doi:10.1029/GM178.

Robigou, V., J. R. Delaney, and D. S. Stakes (1993), Large massive sulfide deposits in a newly discovered active hydrothermal system, The High-Rise Field, Endeavour Segment, Juan De Fuca Ridge, *Geophys. Res. Lett.*, *20*(17), 1887–1890, doi:10.1029/93GL01399.

Rona, P. A., and D. A. Trivett (1992), Discrete and diffuse heat transfer at ASHES vent field, Axial Volcano, Juan de Fuca Ridge, *Earth Planet. Sci. Lett.*, *109*, 57–71.

Rona, P. A., M. D. Hannington, C. Y. Raman, G. Thompson, M. K. Tivey, S. E. Humphris, C. Lalou, and P. Petersen (1993), Active and relict seafloor hydrothermal mineralization at the TAG hydrothermal field, Mid-Atlantic Ridge, *Econ. Geol.*, *88*, 1989–2017.

Rudnicki, M. D., and C. R. German (2002), Temporal variability of the hydrothermal plume above the Kairei vent field, 25°S, Central Indian Ridge, *Geochem. Geophys. Geosyst.*, *3*, doi:10.1029/2001GC000240.

Schultz, A., J. R. Delaney, and R. E. McDuff (1992), On the partitioning of heat flux between diffuse and point source seafloor venting, *J. Geophys. Res.*, *97*, 12,299–12,314.

Sclater, J. G., C. Jaupart, and D. Galson (1980), The heat flow through oceanic and continental crust and the heat loss of the Earth, *Rev. Geophys.*, *18*(1), 269–311, doi:10.1029/RG018i001p00269.

Singh, S. C., W. C. Crawford, H. Carton, T. Seher, V. Combier, M. Cannat, J. P. Canales, D. Dusunur, J. Escartin, and

J. M. Miranda (2006), Discovery of a magma chamber and faults beneath a Mid-Atlantic Ridge hydrothermal field, *Nature*, *442*, 1029–1032.

Sohn, R. A., D. J. Fornari, K. L. Von Damm, J. A. Hildebrand, and S. C. Webb (1998), Seismic evidence and hydrothermal evidence for a cracking event on the East Pacific Rise crest at 9°50′ N, *Nature*, *396*, 159–161.

Spiess, F. N., et al. (1980), East Pacific Rise: Hot springs and geophysical experiments, *Science*, *207*, 1421–1433.

Stein, C. A., and S. Stein (1994), Constraints on hydrothermal heat flux through the oceanic lithosphere from global heat flow, *J. Geophys. Res.*, *99*, 3081–3095.

Thompson, W. J., R. E. McDuff, F. R. Stahr, D. R. Yoerger, and M. Jakuba (2005), Heat flux from the Endeavour segment of the Juan de Fuca Ridge, *Eos Trans. AGU*, 86, Fall Meet. Suppl., Abstract T31A-0489, AGU, Washington, D. C.

Tolstoy, M., F. Waldhauser, D. R. Bohnenstiehl, R. T. Weekly, and W. Y. Kim (2008), Seismic identification of along-axis hydrothermal flow on the East Pacific Rise, *Nature*, *451*, 181–184.

Van Ark, E. M., R. S. Detrick, J. P. Canales, S. M. Carbotte, A. J. Harding, G. M. Kent, M. R. Nedimovic, W. S. D. Wilcock, J. B. Diebold, and J. M. Babcock (2007), Seismic structure of the Endeavour segment, Juan de Fuca Ridge: Correlations with seismicity and hydrothermal activity, *J. Geophys. Res.*, *112*, B02401, doi:10.1029/2005JB004210.

Veirs, S. R., R. E. McDuff, and F. R. Stahr (2006), Magnitude and variance of near-bottom horizontal heat flux at the Main Endeavour hydrothermal vent field, *Geochem. Geophys. Geosyst.*, *7*, Q02004, doi:10.1029/2005GC000952.

Von Damm, K. L., and M. D. Lilley (2004), Diffuse flow hydrothermal fluids from 9°50′N East Pacific Rise: Origin, evolution and biogeochemical controls, in The Subseafloor Biosphere at Mid-Ocean Ridges, Geophys. Monogr. Ser., vol. 144, edited by W. S. Wilcock, E. F. DeLong, D. S. Kelley, J. A. Baross, and S. Craig Cary, 399 pp., AGU, Washington, D. C., doi:10.1029/GM144.

Wankel, S. D., L. N. Germanovich, M. D. Lilley, G. Genc, C. J. DiPerna, A. S. Bradley, E. J. Olson, and P. R. Girguis (2011), Influence of subsurface biosphere on geochemical fluxes from diffuse hydrothermal fluids, *Nat. Geosci.*, *4*, 461–468, doi:10.1038/ngeo1183.

Wilcock, W. S. (2004), Physical response of mid-ocean ridge hydrothermal systems to local earthquakes, *Geochem. Geophys. Geosyst.*, *5*, Q11009, doi:10.1029/2004GC000701.

Wolery, T. J., and N. H. Sleep (1976), Hydrothermal circulation and geochemical flux at mid-ocean ridges, *J. Geol.*, *84*, 249–275.